In vivo volumetric quantitative micro-elastography of human skin

SHAGHAYEGH ES'HAGHIAN,[1,*] KELSEY M. KENNEDY,[1,2] PEIJUN GONG,[1] QINGYUN LI,[1] LIXIN CHIN,[2,3] PHILIP WIJESINGHE,[1,2] DAVID D. SAMPSON,[1,4] ROBERT A. MCLAUGHLIN,[1,5] AND BRENDAN F. KENNEDY[2,3]

[1]*Optical+Biomedical Engineering Laboratory, School of Electrical, Electronic & Computer Engineering, The University of Western Australia, 35 Stirling Highway, Perth, WA 6009, Australia*
[2]*BRITElab, Harry Perkins Institute of Medical Research, QEII Medical Centre, 6 Verdun Street, Nedlands, WA 6009*
[3]*School of Electrical, Electronic & Computer Engineering, The University of Western Australia, 35 Stirling Highway, Perth, WA 6009, Australia*
[4]*Centre for Microscopy, Characterisation & Analysis, The University of Western Australia, 35 Stirling Highway, Perth, WA 6009, Australia*
[5]*Australian Research Council Centre of Excellence for Nanoscale Biophotonics, School of Medicine, Faculty of Health Sciences, University of Adelaide, Adelaide, South Australia, 5005, Australia*
*shaghayegh.eshaghian@research.uwa.edu.au

Abstract: In this paper, we demonstrate *in vivo* volumetric quantitative micro-elastography of human skin. Elasticity is estimated at each point in the captured volume by combining local axial strain measured in the skin with local axial stress estimated at the skin surface. This is achieved by utilizing phase-sensitive detection to measure axial displacements resulting from compressive loading of the skin and an overlying, compliant, transparent layer with known stress/strain behavior. We use an imaging probe head that provides optical coherence tomography imaging and compression from the same direction. We demonstrate our technique on a tissue phantom containing a rigid inclusion, and present *in vivo* elastograms acquired from locations on the hand, wrist, forearm and leg of human volunteers.

References and links

1. R. Muthupillai, D. J. Lomas, P. J. Rossman, J. F. Greenleaf, A. Manduca, and R. L. Ehman, "Magnetic resonance elastography by direct visualization of propagating acoustic strain waves," Science **269**(5232), 1854–1857 (1995).
2. J. Ophir, I. Céspedes, H. Ponnekanti, Y. Yazdi, and X. Li, "Elastography: a quantitative method for imaging the elasticity of biological tissues," Ultrason. Imaging **13**(2), 111–134 (1991).
3. B. F. Kennedy, K. M. Kennedy, and D. D. Sampson, "A review of optical coherence elastography: fundamentals, techniques and prospects," IEEE J. Sel. Top. Quantum Electron. **20**(2), 272–288 (2014).
4. S. Wang and K. V. Larin, "Optical coherence elastography for tissue characterization: a review," J. Biophotonics **8**(4), 279–302 (2015).
5. J. A. Mulligan, G. R. Untracht, S. N. Chandrasekaran, C. N. Brown, and S. G. Adie, "Emerging approaches for high-resolution imaging of tissue biomechanics with optical coherence elastography," IEEE J. Sel. Top. Quantum Electron. **22**(3), 246–265 (2016).
6. K. V. Larin and D. D. Sampson, "Optical coherence elastography - OCT at work in tissue biomechanics [Invited]," Biomed. Opt. Express **8**(2), 1172–1202 (2017).
7. B. F. Kennedy, R. A. McLaughlin, K. M. Kennedy, L. Chin, P. Wijesinghe, A. Curatolo, A. Tien, M. Ronald, B. Latham, C. M. Saunders, and D. D. Sampson, "Investigation of Optical Coherence Microelastography as a Method to Visualize Cancers in Human Breast Tissue," Cancer Res. **75**(16), 3236–3245 (2015).
8. C. Li, G. Guan, Y. Ling, Y.-T. Hsu, S. Song, J. T. J. Huang, S. Lang, R. K. Wang, Z. Huang, and G. Nabi, "Detection and characterisation of biopsy tissue using quantitative optical coherence elastography (OCE) in men with suspected prostate cancer," Cancer Lett. **357**(1), 121–128 (2015).
9. S. Wang and K. V. Larin, "Shear wave imaging optical coherence tomography (SWI-OCT) for ocular tissue biomechanics," Opt. Lett. **39**(1), 41–44 (2014).

10. J. Rogowska, N. A. Patel, J. G. Fujimoto, and M. E. Brezinski, "Optical coherence tomographic elastography technique for measuring deformation and strain of atherosclerotic tissues," Heart **90**(5), 556–562 (2004).
11. J. A. Clark, J. C. Y. Cheng, and K. S. Leung, "Mechanical properties of normal skin and hypertrophic scars," Burns **22**(6), 443–446 (1996).
12. S. J. Kirkpatrick, R. K. Wang, D. D. Duncan, M. Kulesz-Martin, and K. Lee, "Imaging the mechanical stiffness of skin lesions by in vivo acousto-optical elastography," Opt. Express **14**(21), 9770–9779 (2006).
13. B. Kalis, J. De Rigal, F. Léonard, J. L. le Lévêque, O. De Riche, Y. L. Corre, and O. D. Lacharriere, "In vivo study of scleroderma by non-invasive techniques," Br. J. Dermatol. **122**(6), 785–791 (1990).
14. C. Escoffier, J. de Rigal, A. Rochefort, R. Vasselet, J. L. Lévêque, and P. G. Agache, "Age-related mechanical properties of human skin: an in vivo study," J. Invest. Dermatol. **93**(3), 353–357 (1989).
15. C. Li, G. Guan, R. Reif, Z. Huang, and R. K. Wang, "Determining elastic properties of skin by measuring surface waves from an impulse mechanical stimulus using phase-sensitive optical coherence tomography," J. R. Soc. Interface **9**(70), 831–841 (2012).
16. C. Li, G. Guan, X. Cheng, Z. Huang, and R. K. Wang, "Quantitative elastography provided by surface acoustic waves measured by phase-sensitive optical coherence tomography," Opt. Lett. **37**(4), 722–724 (2012).
17. X. Liang and S. A. Boppart, "Biomechanical properties of in vivo human skin from dynamic optical coherence elastography," IEEE Trans. Biomed. Eng. **57**(4), 953–959 (2010).
18. Z. Han, J. Li, M. Singh, C. Wu, C. H. Liu, S. Wang, R. Idugboe, R. Raghunathan, N. Sudheendran, S. R. Aglyamov, M. D. Twa, and K. V. Larin, "Quantitative methods for reconstructing tissue biomechanical properties in optical coherence elastography: a comparison study," Phys. Med. Biol. **60**(9), 3531–3547 (2015).
19. C. Li, G. Guan, Z. Huang, R. K. Wang, and G. Nabi, "Full skin quantitative optical coherence elastography achieved by combining vibration and surface acoustic wave methods," Proc. SPIE **9322**, 93220O (2015).
20. B. F. Kennedy, T. R. Hillman, R. A. McLaughlin, B. C. Quirk, and D. D. Sampson, "In vivo dynamic optical coherence elastography using a ring actuator," Opt. Express **17**(24), 21762–21772 (2009).
21. B. F. Kennedy, X. Liang, S. G. Adie, D. K. Gerstmann, B. C. Quirk, S. A. Boppart, and D. D. Sampson, "In vivo three-dimensional optical coherence elastography," Opt. Express **19**(7), 6623–6634 (2011).
22. K. M. Kennedy, S. Es'haghian, L. Chin, R. A. McLaughlin, D. D. Sampson, and B. F. Kennedy, "Optical palpation: optical coherence tomography-based tactile imaging using a compliant sensor," Opt. Lett. **39**(10), 3014–3017 (2014).
23. S. Es'haghian, K. M. Kennedy, P. Gong, D. D. Sampson, R. A. McLaughlin, and B. F. Kennedy, "Optical palpation in vivo: imaging human skin lesions using mechanical contrast," J. Biomed. Opt. **20**(1), 016013 (2015).
24. V. Y. Zaitsev, L. A. Matveev, A. L. Matveyev, G. V. Gelikonov, and V. M. Gelikonov, "Elastographic mapping in optical coherence tomography using an unconventional approach based on correlation stability," J. Biomed. Opt. **19**(2), 021107 (2014).
25. K. M. Kennedy, L. Chin, R. A. McLaughlin, B. Latham, C. M. Saunders, D. D. Sampson, and B. F. Kennedy, "Quantitative micro-elastography: imaging of tissue elasticity using compression optical coherence elastography," Sci. Rep. **5**, 15538 (2015).
26. Y. Qiu, F. R. Zaki, N. Chandra, S. A. Chester, and X. Liu, "Nonlinear characterization of elasticity using quantitative optical coherence elastography," Biomed. Opt. Express **7**(11), 4702–4710 (2016).
27. B. F. Kennedy, S. H. Koh, R. A. McLaughlin, K. M. Kennedy, P. R. T. Munro, and D. D. Sampson, "Strain estimation in phase-sensitive optical coherence elastography," Biomed. Opt. Express **3**(8), 1865–1879 (2012).
28. K. M. Kennedy, C. Ford, B. F. Kennedy, M. B. Bush, and D. D. Sampson, "Analysis of mechanical contrast in optical coherence elastography," J. Biomed. Opt. **18**(12), 121508 (2013).
29. R. K. Wang, Z. H. Ma, and S. J. Kirkpatrick, "Tissue Doppler optical coherence elastography for real time strain rate and strain mapping of soft tissue," Appl. Phys. Lett. **89**(14), 144103 (2006).
30. B. F. Kennedy, R. A. McLaughlin, K. M. Kennedy, L. Chin, A. Curatolo, A. Tien, B. Latham, C. M. Saunders, and D. D. Sampson, "Optical coherence micro-elastography: mechanical-contrast imaging of tissue microstructure," Biomed. Opt. Express **5**(7), 2113–2124 (2014).
31. P. Gong, S. Es'haghian, K. A. Harms, A. Murray, S. Rea, B. F. Kennedy, F. M. Wood, D. D. Sampson, and R. A. McLaughlin, "Optical coherence tomography for longitudinal monitoring of vasculature in scars treated with laser fractionation," J. Biophotonics **9**(6), 626–636 (2016).
32. G. Lamouche, B. F. Kennedy, K. M. Kennedy, C. E. Bisaillon, A. Curatolo, G. Campbell, V. Pazos, and D. D. Sampson, "Review of tissue simulating phantoms with controllable optical, mechanical and structural properties for use in optical coherence tomography," Biomed. Opt. Express **3**(6), 1381–1398 (2012).
33. T. Gambichler, R. Matip, G. Moussa, P. Altmeyer, and K. Hoffmann, "In vivo data of epidermal thickness evaluated by optical coherence tomography: effects of age, gender, skin type, and anatomic site," J. Dermatol. Sci. **44**(3), 145–152 (2006).
34. J. T. Iivarinen, R. K. Korhonen, P. Julkunen, and J. S. Jurvelin, "Experimental and computational analysis of soft tissue stiffness in forearm using a manual indentation device," Med. Eng. Phys. **33**(10), 1245–1253 (2011).
35. R. Huber, M. Wojtkowski, and J. G. Fujimoto, "Fourier Domain Mode Locking (FDML): a new laser operating regime and applications for optical coherence tomography," Opt. Express **14**(8), 3225–3237 (2006).
36. M. Singh, C. Wu, C. H. Liu, J. Li, A. Schill, A. Nair, and K. V. Larin, "Phase-sensitive optical coherence elastography at 1.5 million A-Lines per second," Opt. Lett. **40**(11), 2588–2591 (2015).

37. K. J. Parker, M. M. Doyley, and D. J. Rubens, "Imaging the elastic properties of tissue: the 20 year perspective," Phys. Med. Biol. **56**(1), R1–R29 (2011).
38. P. Wijesinghe, D. D. Sampson, and B. F. Kennedy, "Computational optical palpation: a finite-element approach to micro-scale tactile imaging using a compliant sensor," J. R. Soc. Interface **14**(128), 20160878 (2017).
39. J. E. Bischoff, E. M. Arruda, and K. Grosh, "Finite element modeling of human skin using an isotropic, nonlinear elastic constitutive model," J. Biomech. **33**(6), 645–652 (2000).
40. L. Dong, P. Wijesinghe, J. T. Dantuono, D. D. Sampson, P. R. T. Munro, B. F. Kennedy, and A. A. Oberai, "Quantitative compression optical coherence elastography as an inverse elasticity problem," IEEE J. Sel. Top. Quantum Electron. **22**(3), 277–287 (2016).
41. S. Es'haghian, P. Gong, L. Chin, K. A. Harms, A. Murray, S. Rea, B. F. Kennedy, F. M. Wood, D. D. Sampson, and R. A. McLaughlin, "Investigation of optical attenuation imaging using optical coherence tomography for monitoring of scars undergoing fractional laser treatment," J. Biophoton. epub ahead of print [doi:10.1002] (2016).
42. P. Gong, L. Chin, S. Es'haghian, Y. M. Liew, F. M. Wood, D. D. Sampson, and R. A. McLaughlin, "Imaging of skin birefringence for human scar assessment using polarization-sensitive optical coherence tomography aided by vascular masking," J. Biomed. Opt. **19**(12), 126014 (2014).

1. Introduction

Optical coherence elastography (OCE) is a method to image the micro-scale mechanical properties of tissue, requiring three main steps: a mechanical load is imparted to the tissue; the tissue deformation is measured using optical coherence tomography (OCT); and a mechanical model of tissue deformation is utilized to form a map of a mechanical property (such as Young's modulus). Advantages of OCE over other elastography techniques, such as magnetic resonance elastography [1] and ultrasound elastography [2], include its higher spatial resolution (10-100 μm), enabling detection of smaller features, and its sensitivity to nano-scale displacements (afforded by phase-sensitive detection [3]), providing the potential for improved sensitivity to changes in mechanical properties. OCE has progressed rapidly over the last few years [4–6] and has been proposed for a range of applications, including in oncology [7, 8], ophthalmology [9] and cardiology [10]. However, to date, the majority of OCE demonstrations have been limited to tissue-mimicking phantoms and excised tissues. For clinical applications in dermatology, it is desirable to develop *in vivo* OCE capabilities to enable objective and non-invasive assessment of diseases that alter the mechanical properties of skin, such as pathological scarring [11], cancer [12] and scleroderma [13], as well as provide a tool to assess skin aging with potential applications in the cosmetics industry [14].

To date, there have been a number of *in vivo* demonstrations of OCE on skin. The OCE techniques used can be divided into two main categories. In one category, surface acoustic waves (SAWs) are introduced to the skin, and the measured phase velocity of the propagating wave is used to estimate the Young's modulus averaged over a certain propagation distance. An advantage of these techniques is that they can provide a direct assessment of the elasticity of skin [15–17], although there are many potential complications [18]. Additionally, SAW methods applied to skin can potentially provide elastograms at depths beyond the OCT imaging depth [16]. However, these methods have been limited to 1D or 2D measurements of skin, and the lateral resolution has been limited to ~0.5 mm by the wavelength of the propagating wave and the sampling density of the OCT measurement [16, 19].

In contrast, another category of OCE methods suitable for *in vivo* application, compression-based methods, have provided higher lateral resolution than SAW methods to date, with demonstrated potential to assess micro-scale variations in the mechanical properties of skin [20–25]. These methods are based on compressive loading, in which mechanical loading and imaging are often performed from the same direction. A limitation of compression combined with OCT imaging, however, is that it provides only strain, which is a relative assessment of tissue elasticity. Kennedy *et al.* demonstrated the feasibility of using compression OCE to 3D map axial strain in human skin *in vivo* [21]. This relative assessment of the elasticity of skin precludes comparison of results acquired from different samples and longitudinal assessment in the same sample.

Recently, we demonstrated an adjunct to the compression-based method, termed optical palpation, in which the change in thickness of a compliant, transparent layer placed between the loading element and the tissue surface is used to map the axial stress at the tissue surface [23]. This 2D map of surface stress provides a qualitative measurement of the elasticity of tissue under the compliant layer at each lateral location. We have demonstrated optical palpation for *in vivo* imaging of human skin lesions (scars and a nevus) [23]. Qiu *et al.* have also recently reported a similar technique and demonstrated it to show the stress-strain relationship of skin *in vivo* [26].

With access to both volumetric axial strain via compression, phase-sensitive OCE, and surface axial stress via optical palpation, we have previously combined the two measurements to achieve an OCE technique that estimates elasticity at high spatial resolution, a form of volumetric, quantitative micro-elastography [25]. In this paper, we demonstrate this method with a suitably modified probe design to achieve the first *in vivo* results using this form of volumetric, quantitative micro-elastography. To demonstrate the technique, we present elasticity images from a skin-mimicking phantom, before showing *in vivo* results from sites on human skin, including the hand, wrist, forearm and leg of human volunteers.

Specifically, this provides a tangent modulus, which is equivalent to Young's modulus only under the assumption that the tissue is linear elastic. Soft tissue is often linear elastic up to strains up to 20% [26], but tends to be hyperelastic in general (increasing elasticity with strain).

2. Methods

2.1 Quantitative micro-elastography

We briefly summarize the method via which we combine volume axial strain with surface axial stress to estimate elasticity, which has been described in detail previously [25]. The local axial strain in the tissue is calculated from local axial displacement caused by the quasi-static load and captured using phase-sensitive compression OCE [27]. A variant of optical palpation is used to measure stress, in which a compliant, transparent silicone layer, with known stress/strain behavior, is placed between the imaging window and the skin [23] (Fig. 1(a)). During imaging, we apply a preload to ensure complete contact of the compliant layer with both the skin and the imaging window. The preload also helps to reduce motion artifact caused by movement of the subject by better coupling of the probe with the area being scanned.

The change in thickness of the layer is used to infer the distribution of axial stress across the compliant layer-skin interface [22]. Under the assumption that the stress at each lateral position is uniform with depth and is uniaxial [28], dividing the stress at the skin surface by the local, axial strain in the tissue volume provides an estimate of the elasticity of skin. Specifically, this provides a tangent modulus, which is equivalent to Young's modulus, under the assumption that the tissue being scanned is linear elastic, which is often the case in soft tissues at strains up to 20% [26]. The strain in the compliant layer brought about by the preload, which we refer to as the bulk strain, $\varepsilon_{bulk}(x, y)$, is measured by dividing the change in layer thickness by the initial thickness at each lateral (x, y) position, $\varepsilon_{bulk}(x, y) = \Delta l(x, y)/l_0(x, y)$, in the field of view. The layer thickness is measured in each OCT B-scan in a volume acquisition using an algorithm based on the Canny edge detector [22]. The stress at each lateral position is then estimated from the stress-strain curve of the compliant layer, which was independently measured using a standard compression test (Instron, Norwood, MA, USA). In the preloaded state, an annular piezoelectric actuator with a maximum stroke of 12 μm, was fixed to the imaging window (12.7 mm diameter) and a step-wise, micro-scale displacement with a frequency of 14 Hz was applied. The actuator motion was synchronized with the OCT B-scan acquisition, such that consecutive B-scans were acquired in different loading states. The phase difference between co-located OCT axial scans

in sequential B-scans was then calculated to obtain the depth-resolved, axial displacement maps of both the compliant layer and the sample [29]. Depth-resolved (*i.e.*, local) axial strain in the sample, $\varepsilon_{sample}(x,y,z)$, is estimated from the axial gradient of displacement in depth using a weighted least-squares fitting algorithm over an axial range of 200 μm [27], which sets the minimum axial spatial resolution of the technique. To extend the range of measurable displacements, a phase unwrapping algorithm, described previously, was employed [27, 30]. The strain in the compliant layer produced by the actuator, $\varepsilon_{layer}(x,y)$, is determined by dividing the displacement determined using phase-sensitive detection at the interface of the layer and the sample, $d_l(x,y)$, by the preloaded thickness of the layer, $l(x,y)$, determined from the OCT image [25], *i.e.*,

$$\varepsilon_{layer}(x,y) = \frac{d_l(x,y)}{l(x,y)}. \tag{1}$$

The increase in stress in the compliant layer due to micro-scale actuation is then assessed from the stress-strain curve at the preload layer strain,

$$\sigma_{layer}(x,y) = E'_{layer}(\varepsilon_{bulk}(x,y)) \times \varepsilon_{layer}(x,y), \tag{2}$$

where $E'_{layer}(x,y)$, referred to as the 'tangent modulus' of the layer, is the derivative of the stress-strain curve, with respect to strain, of the compliant layer. The elasticity (tangent modulus) values of skin are then generated by mapping the ratio of local surface axial stress to local volume axial strain at each pixel,

$$E'_{skin}(x,y,z) = \frac{\sigma_{layer}(x,y)}{\varepsilon_{skin}(x,y,z)}. \tag{3}$$

2.2 Imaging system

Scanning was performed using a commercial, spectral-domain OCT system (TELESTO II, Thorlabs Inc., Newton, NJ, USA) operating at a center wavelength of 1300 nm. Figure 1(a) shows a schematic of the OCT system and the imaging probe. The manufacturer-specified axial resolution of the system is 5.5 μm (in air). To generate results presented in this paper, two scanning lenses were used. One lens (LMS03, Thorlabs), with lateral resolution of 13 μm and working distance of 25 mm, was used for imaging the phantom (Fig. 2) and the *in vivo* scar on the wrist (Fig. 5). All other results (Figs. 3,4,6) were generated using another lens (LMS04, Thorlabs), with lateral resolution of ~20 μm and working distance of 42 mm. The OCT system was operated in a common-path configuration, with the reflected beam from the back surface of the 3 mm-thick glass window in contact with the skin used as a reference reflection, as shown in Fig. 1(a). The conventional reference arm of the system, which is encapsulated within the imaging probe, was blocked by inserting a beam stop in the reference light path. Each OCT B-scan comprised either 700 or 1000 A-scans, acquired with an exposure time in the range 16–28 μs and an A-scan line rate of 28 kHz (period of 36 μs). The data acquisition time varied from ~1 to ~2.5 min for C-scans with dimensions in the range (5-6) × (2-3) × 3 mm in *x*, *y* and *z*, respectively.

Custom acquisition software was used to acquire OCT data and to enable live viewing of the phase difference between adjacent B-scan pairs. This live viewing was important in ensuring that adequate preload was applied to the skin to produce measurable strain. For the phantom and *in vivo* scar scans, 10 pairs of B-scans were recorded at each *y* location to allow temporal averaging, and the sampling density of A-scans in the *x*-direction matched that in the *y*-direction. For all other *in vivo* scans, 2 B-scans were recorded at each *y* location and the

sampling density in the *y*-direction was 4 or 5 times that in the *x*-direction, allowing both temporal and spatial averaging to further improve strain sensitivity.
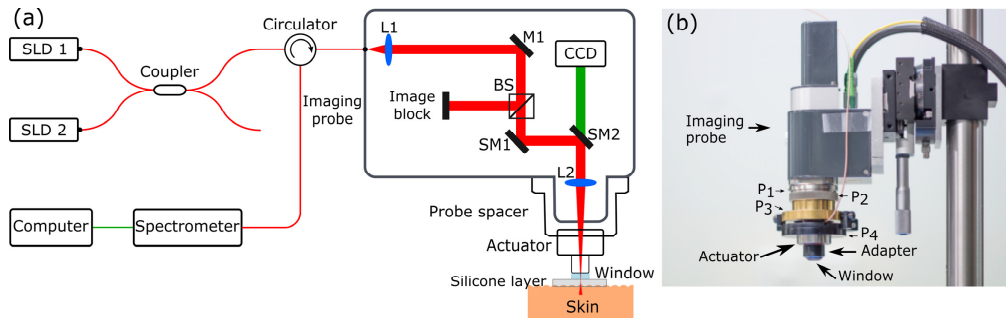

Fig. 1. System used for *in vivo*, volumetric, quantitative micro-elastography. (a) System diagram and (b) photograph of the probe. Abbreviations in (a): BS, beam splitter; CCD, charge-coupled device; L, lens; M, mirror; SLD, superluminescent diode; SM, scanning mirror. P1-P4 in (b) are described in the text.

2.3 *In vivo* imaging probe

An adjustable probe head based on the manufacturer-supplied scan head was designed to provide OCT imaging, compressive pre-loading and quasi-static, micro-scale actuation from the same side of the sample. This probe is an extension and refinement of OCE and microvasculature imaging probes previously developed by our group [23, 31]. A photograph of the probe is shown in Fig. 1(b). The focus of the light illuminating the sample is adjusted using the top section of the probe (two threaded silver rings, P_1 and P_2, and the threaded golden ring, P_3), which is designed to allow the height of the probe to be adjusted. The probe has an adjustable tilt, provided by P_4, which is required to optimize the common-path reference reflection from the imaging window, both to avoid saturation of the detector and to minimize any variation in reference arm power within a B-scan. The actuator (with an outer diameter of 35 mm and a height of 18.2 mm) is connected to the probe using threaded ring P_4, as indicated in Fig. 1. The imaging window is made from uncoated calcium fluoride (CaF_2) (refractive index = 1.427) with thickness of 3 mm and a diameter of 12.7 mm. This window also functions as a compression plate, compressing both the compliant layer and the skin. The entire probe is connected to a translation stage to allow well-controlled preloading of the sample, which, in turn, is connected to a tilt stage to ensure that the compression plate is parallel to the sample. The lateral position of the probe can be moved in *x* and *y*, using two perpendicular translation stages.

2.4 Fabrication and imaging of compliant layer and tissue-mimicking phantom

All compliant, transparent layers and tissue-mimicking phantoms were fabricated from the same silicone material (Wacker, P7676), using procedures outlined previously [23, 32]. The compliant layers were fabricated to have a diameter of 15 mm, a thickness of 0.5-0.8 mm and an elasticity of 6.4 kPa at 10% strain. The tissue-mimicking phantom had a cylindrical shape with a diameter of 25 mm and a thickness of 1.7 mm. The phantom contained a stiff inclusion (135 kPa at 10% strain) fabricated using a second silicone material (Wacker, RT601) in a matrix with an elasticity of 5.5 kPa at 10% strain. The inclusion had dimensions of ~0.8 × 0.7 × 0.5 mm in *xyz* and was located ~0.5 mm below the phantom surface. To introduce optical scattering, titanium dioxide particles with average diameter <1 μm and refractive index ~2.49 were added to both the bulk material (0.8 mg/ml) and the inclusion (2.5 mg/ml). For both the compliant layers and the phantoms, the elastic modulus was measured using a standard compression test (Instron, Norwood, MA, USA). A refractive index of 1.4 is assumed for the both the layer and the phantom.

2.5 In vivo imaging protocol

This study was approved by the University of Western Australia Human Research Ethics Committee. *In vivo*, volumetric, quantitative micro-elastography was carried out on four human volunteers (all Caucasian, three males and one female). We present images acquired from the fingertip, the dorsal forearm, the lateral wrist, and the anterior medial leg, including two skin lesions: a nevus and a scar. The steps taken prior to imaging were similar to those used for *in vivo* optical palpation [23]. This involved taking photographs of the imaging location and marking it, shaving the hair at the imaging location to reduce shadowing artifacts in OCT imaging, and lubricating both sides of the compliant layer and the skin location with silicone fluid before positioning the layer on the skin surface to minimize friction. Additionally, steps were taken to minimize discomfort to the patient, including positioning the skin on cushions and ensuring that the subject was in a comfortable position. This helped to reduce motion artifact in the micro-elastograms. The probe head was brought into contact with the compliant layer and skin, and the preload was incremented until the 2D phase-difference image, observed in real-time, was free of motion artifacts. We observed a reduction in motion artifact with increasing preload, which we attribute to the reduced ability of the tissue under load to move relative to the imaging probe. Once these steps had been completed, micro-actuation commenced and OCT imaging was performed.

In the micro-elastograms of skin, we have masked out regions in which positive strain (*i.e.*, strain in opposition to the direction of applied force) was measured in either the sample or the compliant layer. The B-scan and *en face* micro-elastograms are averaged over 30 μm in z and y directions, respectively, to reduce the effects of noise. This averaging corresponds to averaging over 4-5 pixels in x and 3-5 pixels in y, based on the sampling density used and 9 pixels in z. Similarly to previous demonstrations [7, 25], the B-scan and *en face* micro-elastograms are overlaid on the OCT images, which are visible in the masked-out regions. The *en face* OCT images and micro-elastograms of the *in vivo* results correspond to a physical depth, as reported in each case, beyond the interface of the compliant layer and the skin surface, assuming a refractive index of 1.43 for skin. Because there is a slight mismatch between the refractive index of the compliant layer (1.4) and that expected for skin tissue (1.43 [33]), we chose to present the depth in the B-scan OCT images and elastograms as an as-measured optical path length.

3. Results

3.1 Phantom

Figure 2(a) shows an OCT B-scan in which the compliant layer, the bulk phantom material and the inclusion below the phantom surface are readily distinguished due to their varying scatterer concentrations. An *en face* OCT image, taken from the same data set as the B-scan in Fig. 2(a) at a depth of 0.76 mm from the lower surface of window, is presented in Fig. 2(b). Again, the inclusion is clearly visible in this image. The corresponding micro-elastograms are presented in Figs. 2(c) and 2(d). In Fig. 2(d), the mean elasticity values for the inclusion and the bulk material over an area of 0.5×0.5 mm are 87.5 kPa and 5.8 kPa, respectively. The elasticity of the bulk material corresponds well (<5% error) with that measured independently using a standard compression test (5.5 kPa). However, the elasticity of the stiff inclusion appears to be underestimated compared to the 135 kPa measured by the standard compression test. This discrepancy may be explained by a lower preload strain in the experiment on the inclusion compared with the 10% strain used in the standard compression test, corresponding to a lower tangent modulus for the inclusion in the experiment. In the B-scan micro-elastogram in Fig. 2(c), the layer is masked from the image (black area at top of image).
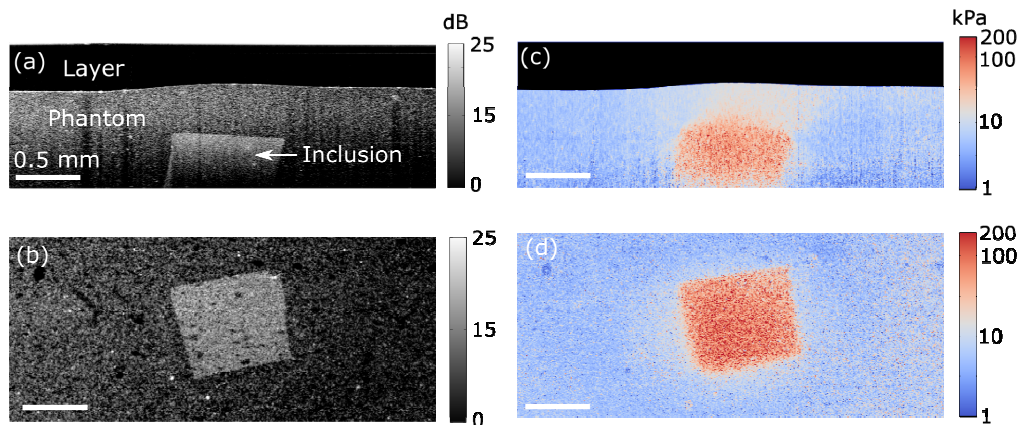
Fig. 2. Quantitative micro-elastography results from the tissue-mimicking phantom. (a) OCT B-scan. (b) *En face* OCT from a depth of 0.76 mm from the zero optical path length. (c) B-scan micro-elastogram (log scale). (d*) En face* micro-elastogram (log scale).

3.2 Case study 1: fingertip

The fingertip on the middle finger of a 26-year old Caucasian male was imaged using the *in vivo* probe. The OCT B-scan and *en face* views are shown in Figs. 3(a) and 3(b), respectively. In Fig. 3(a), the expected layers of skin tissue are readily distinguished: stratum corneum (SC in the image) at the top, the living section of the epidermis (E), and the dermis (D). The location of the B-scan is indicated by the white dashed line in the *en face* view, Fig. 3(b). The corresponding B-scan and *en face* micro-elastograms are overlaid on the OCT images (Figs. 3(c) and 3(d), respectively). The *en face* micro-elastogram in Fig. 3(d) corresponds to a physical depth of 300 μm beyond the interface of the compliant layer and the skin surface, in the epidermis. The elastogram matches well with the corresponding OCT image in Fig. 3(b), showing a pattern of varying elasticity corresponding to the ridges in the OCT image caused by the fingerprint. Additionally, in the B-scan micro-elastogram in Fig. 3(c), variation of elasticity is observed versus depth, corresponding to the different layers of thick skin visible in Fig. 3(a): stratum corneum, epidermis and dermis. The average elasticity values in the white rectangles shown in Fig. 3(c) are, respectively, 299 kPa, 115 kPa and 402 kPa, from top to bottom. These values are of the same order of magnitude as those reported previously for skin [34], and higher elasticity is estimated in the stratum corneum than in the living epidermis, consistent with previous measurements using strain-based compression OCE [21]. However, a direct comparison is not possible with results acquired using point or bulk measurement techniques, which report an average elasticity of multiple skin layers. The accuracy of the elasticity values is also influenced by the axial resolution of micro-elastograms (~200 μm here), which is degraded relative to the resolution of the corresponding OCT images. As a result, at the boundaries between skin layers, the estimated elasticity is also influenced by adjacent axial layers. Such effects are referred to as partial volume effects. For instance, the elasticity measured for the stratum corneum layer may be underestimated due to the softer lower cellular layers of the epidermis. Nevertheless, as expected, higher elasticity is observed in the superficial keratinized nonliving layer of epidermis, the stratum corneum, compared to the lower cellular layers of epidermis [21].
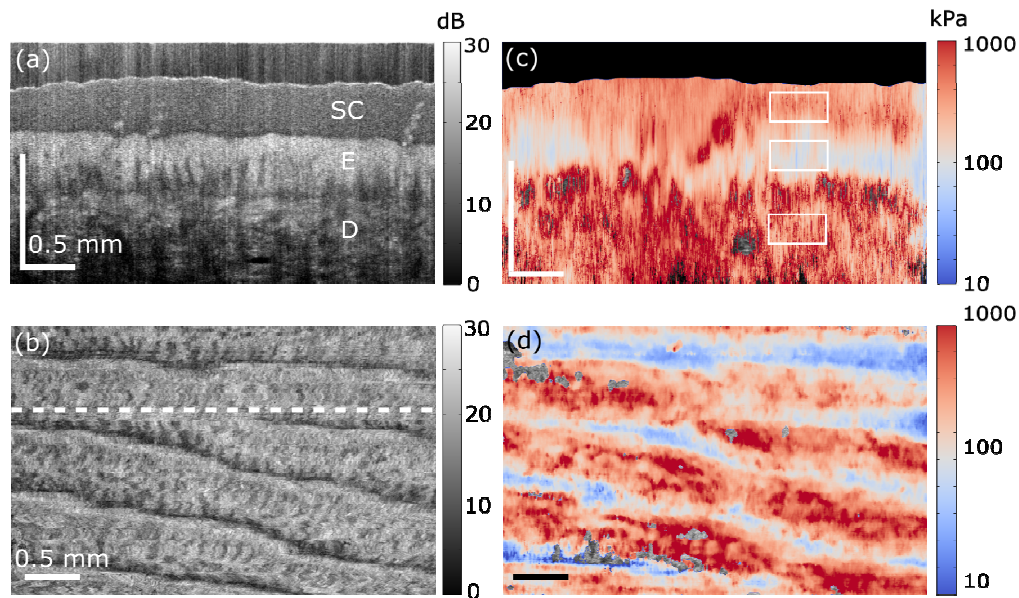
Fig. 3. *In vivo* quantitative micro-elastography results from a fingertip. (a) OCT B-scan. SC, E and D in the image indicate stratum corneum, living epidermis, and dermis, respectively. The scale bar is 0.5 mm in both dimensions, but in depth indicates optical path length. (b) *En face* OCT image, 300 μm (physical length) beyond the interface of the compliant layer and the skin surface. The white dashed line indicates the B-scan location presented in (a). (c) B-scan micro-elastogram. (d) *En face* micro-elastogram, 300 μm (physical length) beyond the interface of the compliant layer and the skin surface, overlaid on the *en face* OCT.

3.3 Case study 2: mole on forearm

Figure 4 shows *in vivo* quantitative micro-elastography results acquired from a mole on the forearm of a 31-year-old female subject. A photograph of the mole is shown in Fig. 4(a). The location of the mole is indicated in the OCT B-scan and *en face* images shown in Figs. 4(b) and 4(c), respectively. The corresponding micro-elastograms are shown in Figs. 4(d) and 4(e). The *en face* micro-elastogram in Fig. 4(e) corresponds to a location in the dermis, 185 μm beyond the interface of the compliant layer and the skin surface. The images in Fig. 4 show that the elasticity of the mole is higher than that of the normal skin. There is a hair follicle in the mole region, (marked as HF) in Fig. 4(c), over which higher elasticity is detected. In Fig. 4(d), the average elasticity values of the normal skin and mole in the dermis over an area of 1 mm in *x* and 200 μm in *z,* were calculated to be ~143 kPa and 223 kPa, respectively.
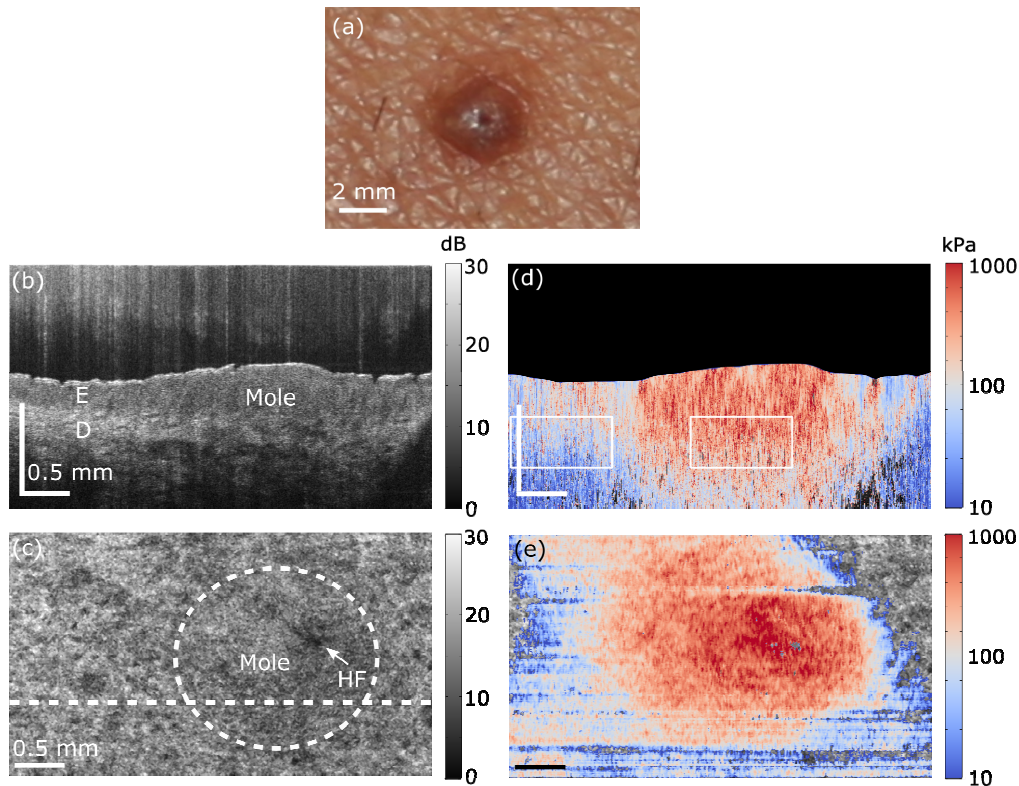
Fig. 4. *In vivo* quantitative micro-elastography results from a mole on the forearm. (a) Photograph of mole. (b) OCT B-scan. The scale bar in depth indicates optical path length. E, living epidermis; D, Dermis. (c) *En face* OCT image, 185 μm (physical length) beyond the interface of the compliant layer and the skin surface. HF shows the prominent position of a hair follicle. White dashed line shows the B-scan location presented in (b) and circular white dashed line shows the approximate location of mole. (d) B-scan micro-elastogram overlaid on the OCT B-scan. (e) *En face* micro-elastogram, 185 μm (physical length) beyond the interface of the compliant layer and the skin surface, overlaid on the *en face* OCT.

3.4 Case study 3: burn scar on the wrist

Figure 5 shows results acquired from a mature burn scar on the wrist above the radius bone of a 34-year old Caucasian male. A photograph of the scar is shown in Fig. 5(a). The outline of the scar is highlighted by a dashed green line and the region scanned using OCT and OCE is indicated by a red box. Figures 5(b) and 5(c) show, respectively, the OCT B-scan and *en face* OCT images. In the *en face* image, higher OCT signal can be seen in the scarred region, as reported previously [23]. The OCT B-scan corresponding to the dashed white line in Fig. 5(c) is shown in Fig. 5(b). In this image, a raised topology is visible in a nodule located within the scarred region. The corresponding micro-elastograms are shown in Figs. 5(d) and 5(e). The *en face* micro-elastogram (Fig. 5(e)) delineates the scarred region with higher contrast than the corresponding *en face* OCT image (Fig. 5(c)). In this micro-elastogram, the scarred region has a higher elasticity than the surrounding unscarred tissue. In the micro-elastogram B-scan (Fig. 5(d)), higher elasticity in the scar is also apparent, particularly over the raised nodule within the scar. This result is consistent with our previous optical palpation results on the same scar [23]. In this previous work, a higher stress was measured in this region, which is indicative of higher elasticity. However, this elasticity difference could not be quantified because of insufficient normal skin within the field of view in Fig. 5. The overall elasticity reported in Fig. 5 is lower than that presented in Figs. 3, 4 and 6 (note the scale differences), indicating the intrinsic variation in skin stiffness between different subjects and skin regions.
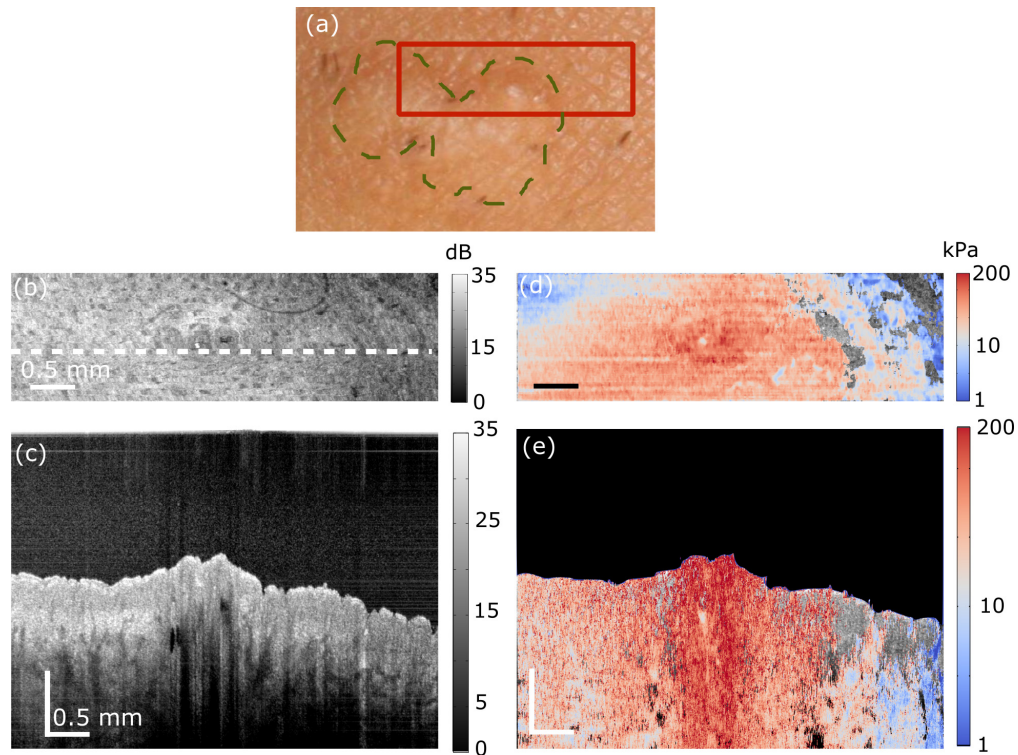
Fig. 5. *In vivo* quantitative micro-elastography results from a burn scar on the wrist over the radial bone. (a) Photograph of the scar. Dashed green line delineates the scar border and the red box shows the region scanned. (b) OCT B-scan. The scale bar in depth represents optical path length. (c) *En face* OCT image, 100 μm (physical length) beyond the interface of the compliant layer and the skin surface. White dashed line shows the B-scan location presented in (b). (d) B-scan micro-elastogram overlaid on the OCT B-scan. (e) *En face* micro-elastogram, 100 μm (physical length) beyond the interface of the compliant layer and the skin surface, overlaid on the *en face* OCT.

3.5 Case study 4: leg (shin)

To demonstrate further the diverse applicability of our probe, we performed *in vivo* quantitative micro-elastography on skin located on the lower limbs. Figure 6 presents images acquired from the medial anterior leg of a 28-year old Caucasian male, allowing comparison with the results from the wrist and forearm already presented. An OCT B-scan and *en face* OCT image are shown in Figs. 6(a) and 6(b), respectively, and the corresponding micro-elastograms are shown in Figs. 6(c) and 6(d). The *en face* micro-elastogram in Fig. 6(d) corresponds to a physical depth of 100 μm beyond the interface of the compliant layer and the skin surface, in the dermis. The average elasticity of the dermis in Fig. 6(c) is ~207 kPa and the average elasticity of the full cross-section of skin in the B-scan in Fig. 6(d) is ~268 kPa. These average values are higher than the elasticity measured in the forearm using *in vivo* quantitative micro-elastography (143 kPa, Fig. 4). This variation warrants further investigation and could potentially be due to varying levels of skin hydration and exposure to sun in the lower limbs.
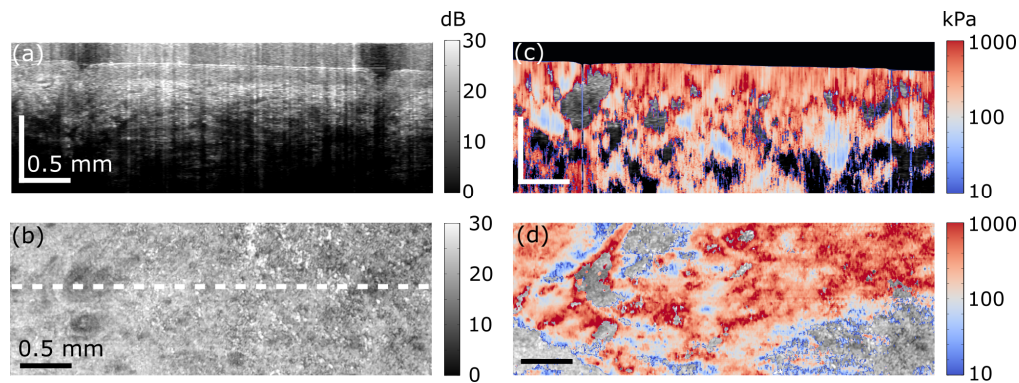
Fig. 6. *In vivo* quantitative micro-elastography results from skin of the anterior medial leg. (a) OCT B-scan. The scale bar in depth represents optical path length. (b) *En face* OCT image, 100 μm (physical length) beyond the interface of the compliant layer and the skin surface. White dashed line shows the B-scan location presented in (a). (c) B-scan micro-elastogram overlaid on the OCT B-scan. (d) *En face* micro-elastogram, 100 μm (physical length) beyond the interface of the compliant layer and the skin surface, overlaid on the *en face* OCT.

4. Discussion

In this paper, we have presented *in vivo,* volumetric, quantitative micro-elastography in human skin. The combination of phase-sensitive, compression OCE with optical palpation in an *in vivo* setting required a number of modifications to our imaging protocols. The contact area between the probe and the skin was reduced to 12.7 mm diameter, and we employed a piezoelectric actuator with greater stroke than used previously (12 μm vs 2-3 μm) [25]. These modifications increased the force applied at the skin surface, which allowed sufficient compression of the layer and skin to generate micro-elastograms with sufficient signal-to-noise ratio. Greater applied force also helped to minimize artifacts caused by underlying, stiff features such as bone and ligaments. Another modification of our probe is the ability to vary the angle between the imaging window and the skin. As this interface acts as the reference reflection, this feature provides a means to control the reference arm power to optimize OCT sensitivity.

The common-path configuration was chosen for this study as it minimizes phase noise in phase-sensitive detection, as we have previously demonstrated [30]. As the sample and reference signals traverse largely common paths, any phase noise caused by, for example, motion or vibration is common to both signals and, therefore, does not affect the phase difference measurement used to estimate displacement. A common-path configuration limits the independent control of sample and reference arm polarizations, which may cause issues, such as a lower OCT SNR, in some samples. However, we did not see any adverse effects in the results presented in this paper. In future, we aim to incorporate bulk motion correction to improve the accuracy of phase-sensitive displacement measurements. In this first demonstration of *in vivo* quantitative micro-elastography, bulk motion correction was rendered unnecessary due to great care in avoiding motion artifact, which may not be achieved in all clinically relevant scenarios.

The acquisition time for the images presented in this paper was ~1-2.5 min per volume, depending on the sampling density. This is much longer than the minimum volumetric OCT data acquisition time because *in vivo* elastography requires dense oversampling to ensure adequate micro-elastogram quality. Clinical translation of *in vivo* quantitative micro-elastography of skin will likely require the development of systems with more rapid acquisition times. This could be achieved by utilizing swept-source OCT systems based on Fourier domain mode-locked (FDML) lasers that provide acquisition times an order of magnitude faster than demonstrated here [35]. Whilst the phase stability of such OCT systems

may impact on micro-elastogram quality, such systems have already demonstrated adequate phase stability in elastic wave propagation-based OCE methods [36].

A general issue with *in vivo* compression-based elastography measurements, and one that has been widely reported in ultrasound elastography [37], is the variation in strain brought about by changes in the load applied to the tissue surface caused by patient movement and/or the environment. Our method, to some extent, accounts for this, as our compliant layer allows us to measure the stress in a dynamic manner, *i.e.*, use of the compliant layer accounts for temporal variations in preload brought about by user and patient motion.

There are implicit assumptions of uniform and uniaxial stress with depth in combining depth-resolved axial strain measurements with surface axial stress measurements to accurately estimate elasticity. In general, uneven tissue surface topography, friction at the surface and macro-scale heterogeneity will reduce accuracy [28, 38], whilst micro-scale heterogeneity, such as blood vessels, may lead to local artifacts in the micro-elastograms [7]. The accuracy of elasticity estimation using quantitative micro-elastography, was calculated to be within 8% of the actual elasticity on phantoms with known elasticity [25]. In the case of skin, stiff regions beyond the imaging range of the system, *e.g.*, bone, can affect the level of preload on the skin within our field-of-view and, due to the non-linear stress-strain response of skin [26, 39], different elasticity values may be measured in regions that may have the same intrinsic mechanical properties. However, since the compliant layer provides an estimate of preload stress, the presence of non-uniform preloading can be identified, as we have recently demonstrated [38]. This information can, therefore, be incorporated into the analysis of the micro-elastograms. Further, this effect is reduced by reducing the diameter of the probe in contact with the skin. The stress applied over a smaller surface area is laterally dissipated more rapidly with depth, such that the influence of the features far outside of the field-of-view is reduced. In the compliant layer, where mechanical properties are well characterized, the effects of friction and uneven stress may be recovered though a computational approach [38]; however, to recover the accuracy of elasticity in heterogeneous tissues requires a computational inverse method [40].

The axial resolution of the micro-elastograms is limited by the depth range over which linear regression to displacement is performed to estimate strain; here, we used 200 μm. The lateral resolution is limited by the OCT system lateral resolution, 13 μm and more here. Additionally, we performed averaging with a kernel size of 30 μm in the *x*, *y* and *z* directions in the micro-elastogram images presented here, which further reduces the lateral and axial resolution of our results. Furthermore, the incompressibility of the silicone material used to fabricate layers can also affect the ability to resolve feature boundaries, especially at depth, as seen in our previous studies [22, 23, 25, 38], and here as a loss of sharpness at feature edges of the inclusion in the micro-elastogram image in Fig. 2(c) compared with the sharper edges of the inclusion in the B-scan OCT image in Fig. 2(a).

Micro-elastograms are presented here in false color overlaid on grayscale OCT, following the procedure we have outlined previously [25]. In this approach, regions in which positive strain (opposite to the direction of applied force) was measured, in either the sample or the layer, are masked out in the overlay image. Positive strain, as described previously [7], arises principally due to non-uniform stress distribution in the tissue generated by local variations in compressibility. In skin, this can be caused by incomplete contact with the compliant layer, created by an uneven surface, which is commonly encountered, as well as by structural and mechanical heterogeneity.

The images presented here were acquired with an OCT system employing a common-path interferometer for which an artifact image is visible in each OCT scan close to the zero path length difference. This artifact is caused by strong backscattering at the interface between the compliant layer and the skin, which acts, in effect, as a second reference arm. To minimize this effect, we set the focus below the tissue surface, however, due to the long working distances of the lenses used, and the corresponding long Rayleigh range, it was not possible to

completely remove this artifact. However, its effects are minor in the results presented here, as the artifact appears to originate within the compliant layer and, as such, is easily visually differentiated from the true skin image.

A direct comparison between the elasticity values estimated for skin samples here and those reported previously in the literature using point or bulk compression techniques is not straightforward. The main reason for this is that existing techniques typically report an average elasticity from all skin layers as well as potentially being affected by the elasticity of the underlying subcutaneous fat. Further, they may operate at a different preload applied to the skin, which is usually not reported, making accurate comparison impossible. In future, non-linear elasticity could be measured with OCE [26], and enable a more direct comparison with other techniques.

Our results demonstrate the capability of our method to estimate the volumetric elasticity of human skin *in vivo*, on the micro-scale. An important next step is to perform pilot clinical studies to determine if this method has the required sensitivity to distinguish regions of pathological tissue. One attractive application of this method is the evaluation of the stiffness of burn scars, further extending our OCT-based approaches to quantify the structure and microvasculature of burn scars [31, 41, 42]. An exciting future possibility is the combination of these methods to perform a more comprehensive characterization of the micro-scale physical properties of skin than has been performed to date.

5. Conclusion

We have presented an *in vivo*, volumetric assessment of the elasticity of human skin on the micro-scale, achieved by combining axial strain measured using volumetric phase-sensitive compression OCE with axial stress measured at the skin surface using a thin, transparent, compliant layer. We have presented results from skin sites of human volunteers including: finger, forearm, leg and wrist of human volunteers. The acquisition time for our technique was ~1-2.5 minutes to scan volumes with dimensions in the range $(5-6) \times (2-3) \times 3$ mm, and the axial and lateral resolution of the technique were ~200 μm and 30 μm, respectively. The results presented here pave the way for future clinical studies.

Funding